

1 Mass diffusion and Soret coefficient measurements of triethylene 2 glycol/water binary mixtures by dynamic shadowgraphy

3 A.T. Ndjaka^{a,b}, L. García-Fernández^c, D. E. Bouyou Bouyou^a, A. Lassin^b, M. Azaroual^{b,d},
4 F.Croccolo^a, H. Bataller^{a*}

5 ^aUniversite de Pau et des Pays de l'Adour, E2S UPPA, CNRS, TotalEnergies, LFCR
6 UMR5150, Anglet, France

7 ^bBRGM, F-45060 Orléans, France

8 ^cDepartment of Structure of Matter, Thermal Physics and Electronics, Faculty of Physics,
9 University Complutense of Madrid, Avda. Complutense s/n, 28040 Madrid, Spain

10 ^dUniv. Orléans, CNRS, BRGM, ISTO, UMR 7327, F-45071, Orléans, France

11 * Corresponding author: henri.bataller@univ-pau.fr
12

13 Abstract

14 The investigation of the transport properties of binary fluid mixtures remains a topic of
15 interest in relation to the more challenging studies of ternary mixtures. In fact, the study of the
16 phase boundary limits of the Gibbs composition triangle can be the initial step for a more
17 complete analysis of ternary mixtures. In this paper, we apply the dynamic shadowgraphy
18 optical technique to study non-equilibrium fluctuations induced by the presence of a gradient
19 of temperature and/or of concentration in the triethylene glycol (TEG)/water system. These
20 thermodiffusion and free-diffusion experiments aim at measuring the transport properties of
21 samples of the studied system at different experimental conditions. We scan both the average
22 temperature and the TEG concentration, which allows us investigating both positive and
23 negative thermodiffusive behaviours. The obtained values of mass diffusion coefficient are
24 consistent with data available in the literature in the range of temperature investigated in this
25 study. The mass diffusion coefficient of the sample prepared at 0.7 w/w TEG concentration
26 are characterised by shadowgraphy following the two proposed methods, exhibiting consistent
27 results. An increase of the mass diffusion coefficient as a function of the average temperature

28 is highlighted. On the other hand, the thermodiffusion coefficient appears to be independent
29 of the average temperature of the sample at 0.3 w/w TEG concentration.

30

31 **1. Introduction**

32 The transport properties of complex fluids under non-equilibrium conditions are of interest
33 from both scientific and technological points of view. Transport phenomena occurs in almost
34 any multicomponent mixture present in nature and in industry and its comprehension is of
35 great interest for many applications, such as the exploitation of crude oil wells and the storage
36 of CO₂ in deep brine aquifers. [1], [2]. A suitable characterization of transport processes in
37 complex mixtures requires a thorough understanding of simpler fluids. So far, binary mixtures
38 have been extensively characterized [3], [4]. The extension of theories and experiments from
39 binary to ternary mixtures requires further development due to the intrinsic and significant
40 increase of difficulty with the number of components of the mixture and their mutual
41 interactions. Currently, a great effort is devoted to investigate the transport phenomena in
42 ternary mixtures. Thermodiffusion experiments in ternary mixtures are performed on ground,
43 by using different optical techniques [3], [5]–[7], or in microgravity conditions in order to
44 avoid both convection and sedimentation. The thermodynamic characterization of ternary
45 mixtures is one of the objectives of different ESA projects, like: Diffusion Coefficient
46 Measurements in ternary mIXtures (DCMIX) [7]–[11], Soret Coefficients in Crude Oil
47 (SCCO) [12]–[15] and Giant Fluctuations [16], [17]. The knowledge of the behavior of the
48 binaries associated to the ternaries remains an important step because they correspond to the
49 binary phase boundary limits in the ternary Gibbs composition triangle, and interpolated
50 values of the Soret coefficient can be obtained in some conditions [18].

51 Complex fluids subjected to non-equilibrium conditions exhibit non-equilibrium fluctuations
52 (NEFs) of the thermodynamic variables [19]–[23]. These conditions can be induced, for

53 example, by applying a temperature gradient to a multicomponent fluid mixture, thus
54 inducing a temperature gradient within the fluid as well as a composition gradient by means
55 of thermodiffusion, also called the Soret effect [3], [24]. Superimposing two layers at
56 different concentrations of a solution generates an initial gradient of concentration which
57 evolves towards an equilibrium state by mass diffusion, in the absence of convective motions
58 [25]. Both free-diffusion and thermodiffusion transport processes can be investigated by
59 optical techniques and particularly by light scattering thanks to its ability to visualize NEFs
60 without altering the intrinsic properties of the fluid. The transport properties of the fluid can
61 be determined both at atmospheric [26], [27] and at high pressure [28]. In this work, dynamic
62 shadowgraphy has been adopted [25], [29], [30] to study the refractive index fluctuations as
63 generated by the NEFs of the temperature and concentration in the case of thermodiffusion
64 experiments, and of the concentration in the case of free-diffusion experiments. It is important
65 to highlight the novelty of using this methodology to determine the transport properties of
66 fluid mixtures in free-diffusion experiments. By shadowgraphy, a large range of fluctuation
67 sizes λ or, conversely, of wave numbers $q = 2\pi/\lambda$, can be investigated at the same time,
68 providing simultaneous reliable measurements of different transport properties, like mass
69 diffusion coefficient or thermal diffusivity as well as Soret coefficient [5], [26], [31].

70 The aim of the present work is to investigate the diffusion and the thermodiffusion
71 coefficients of the binary mixture of triethylene glycol (TEG) and water (H₂O), as one of the
72 binary limits of the DCMIX3 ternary system, made of H₂O, ethanol and TEG [11]. These
73 molecules are highly polar, and the prevailing hydrogen bonding leads to much more complex
74 interactions than the dominating dispersion interactions in alkane mixtures for example,
75 leading to negative values of the Soret coefficient and to convective instabilities under
76 terrestrial gravity conditions. In this study, it is worth noting the possibility of characterising

77 mixtures with negative Soret coefficients through the analysis of NEFs by using shadowgraph
78 technique in both thermodiffusion and free-diffusion experiments.

79 The remainder of this paper is organized as follows: in section 2, the experimental procedure
80 is described. In section 3, the theory of non-equilibrium fluctuations is summarized to provide
81 the relevant working equations. The obtained results are presented in section 4, finally,
82 conclusions are provided in section 5.

83 2. Experimental procedure

84 2.1. Solutions preparation and characterisation

85 Triethylene glycol (Sigma-Aldrich, T59455-1L, ReagentPlus®, purity 99%), used without
86 further purification, and degassed de-ionized water (resistivity 18.5 MΩcm), retrieved from a
87 Millipore Milli-Q filtration station, were used to prepare the studied samples at the required
88 mixture compositions using an analytical balance (Sartorius TE313S, resolution 10⁻² g/200 g).
89 The thermophysical properties of the mixture, such as density, viscosity and both thermal and
90 mass expansion coefficients are measured as follows.

91 The kinematic viscosity ν is measured at 20, 25 and 30 °C by capillary viscometer
92 (Ubbelohde SCHOTT). The thermal and solutal expansion coefficients α and β , respectively,
93 are defined as follows:

$$\alpha = -\frac{1}{\rho} \left(\frac{\partial \rho}{\partial T} \right)_{C,p} \quad (1)$$

$$\beta = \frac{1}{\rho} \left(\frac{\partial \rho}{\partial C} \right)_{T,p} \quad (2)$$

94 where ρ is the mixture density, T is the temperature and C is the TEG concentration in mass
95 fraction.

96 The coefficients α and β are indirectly determined from measurements of the mixture density
 97 performed at different conditions through a Density Meter (ANTON PAAR, DMA 5000).
 98 First, in order to determine the thermal expansion coefficient, the density is measured at
 99 different temperatures (starting from 2 °C below the nominal temperature up to 2 °C above),
 100 while keeping the concentration constant. A linear relationship between the density and the
 101 temperature is observed in all cases. The parameter α is determined through Eq. (1), i.e.
 102 dividing the slope of the density vs. temperature by the density of the sample at the nominal
 103 temperature. Second, the mass expansion coefficient is obtained after measuring the density at
 104 different concentrations (starting from 2% w/w below the nominal concentration up to 2%
 105 w/w above), while keeping the temperature constant. A linear relationship between the
 106 density and the concentration is observed in all cases. The parameter β is determined through
 107 Eq. (2), i.e. dividing the slope of the density vs. concentration by the density of the sample at
 108 the nominal concentration. Measured values of ν , α and β are summarized in Table 1.

109 **Table 1. Kinematic viscosity ν , thermal expansion coefficient α and solutal expansion coefficient β at**
 110 **different both mass fraction concentrations C of TEG and temperatures T .**

T (°C)	ν (mm ² /s)	α ($\times 10^{-4}$ K ⁻¹)	β ($\times 10^{-1}$)
$C = 0.3$ w/w			
20	2.72 ± 0.03	4.22 ± 0.02	1.59 ± 0.08
25	2.32 ± 0.02	4.49 ± 0.02	1.55 ± 0.07
30	2.01 ± 0.02	4.77 ± 0.02	1.51 ± 0.07
$C = 0.5$ w/w			
20	6.25 ± 0.06	5.77 ± 0.01	0.145 ± 0.009
25	5.20 ± 0.05	5.87 ± 0.01	0.138 ± 0.005
30	4.34 ± 0.04	6.02 ± 0.01	0.134 ± 0.003
$C = 0.7$ w/w			

20	14.8 ± 0.1	6.633 ± 0.007	0.96 ± 0.02
25	11.9 ± 0.1	6.712 ± 0.004	0.949 ± 0.006
30	9.7 ± 0.1	6.799 ± 0.005	0.938 ± 0.008

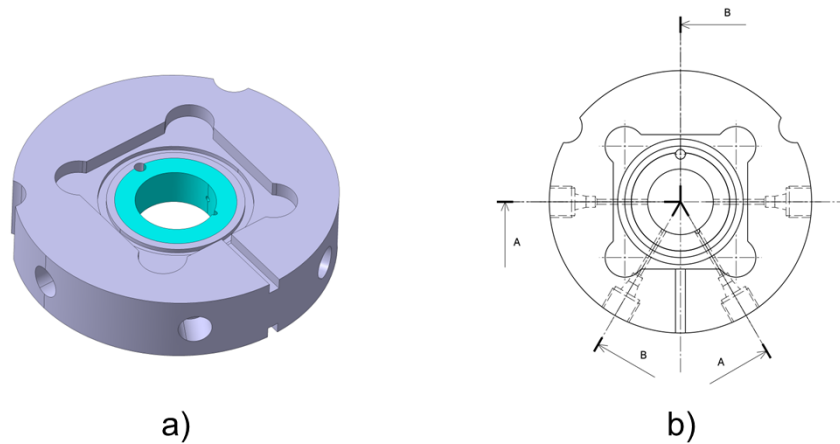
111

112 The measurements of viscosity and density are repeated at least three times for each sample.
 113 The viscosities reported in Table 1 are calculated as the average of the three measurements
 114 and the corresponding uncertainties are the standard deviations. Considering the density
 115 uncertainties and the sensitivity of the method of least-square adjustment, the uncertainties on
 116 α and β are calculated by error propagation.

117 **2.2. Free-diffusion and thermodiffusion cells**

118 For the free-diffusion experiments, we used a diffusion cell specifically designed to put into
 119 contact two layers of two different liquid mixtures or two solutions of the same components at
 120 different concentrations, thus creating an initial step concentration gradient at uniform
 121 temperature while providing vertical optical access to a central area of the cell, similar to the
 122 flowing-junction cell already reported in literature [32]. The diffusion cell consists of a
 123 stainless steel annulus (see Fig. 1) with internal and external diameters of 30 mm and 80 mm,
 124 respectively, and a vertical thickness of $h = 10$ mm. The metallic annulus hosts four holes:
 125 two for fluids outlets at 180° in the horizontal plane and at mid-height of the cell in the
 126 vertical direction, and two for fluid inlet at 50° in the horizontal plane and at the same height
 127 in the vertical direction. In order to avoid the thermal contact between the liquid sample and
 128 the interior of the conductive metallic annulus, a polytetrafluoroethylene (Teflon®) ring with
 129 an internal and external diameter of 20 mm and 30 mm, respectively, is placed inside the
 130 stainless steel annulus (see Fig. 1a) . This ring has also four thin holes in correspondence to
 131 those present in the metallic annulus to allow the circulation of the fluids. Moreover, the two

132 holes for the fluid inlets are inclined in the vertical direction so that one incoming fluid is
133 steered to the top of the cell, while the other one is steered to the bottom of the cell.



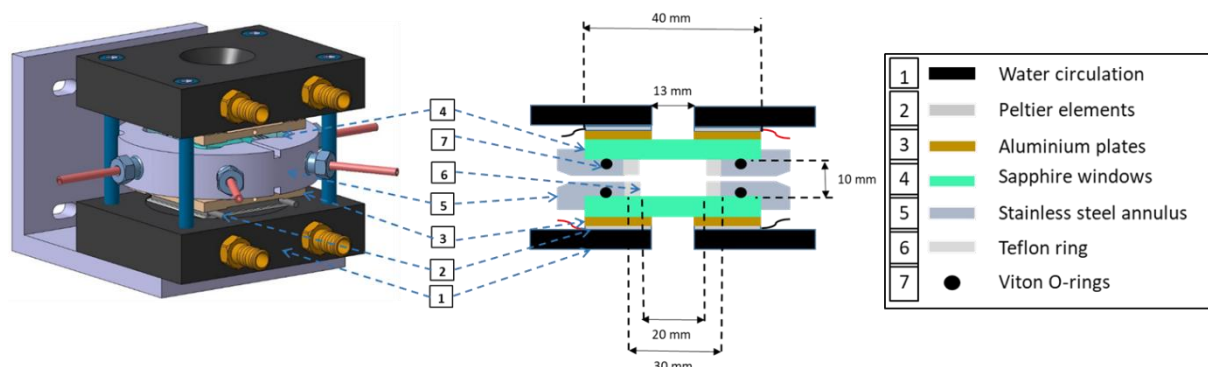
134

135 **Figure 1: a) 3D-drawing of the stainless steel annulus with the Teflon ring in the inner part. b) 2D-**
136 **drawing of the same, as observed from the top.**

137

138 The stainless steel annulus is designed to accommodate two square sapphire windows
139 ($8 \times 40 \times 40$ mm³), one on each vertical side with a groove for a Viton® O-ring for sealing. The
140 two internal faces of the two sapphire windows are then separated by the metal annulus and
141 kept apart by $h = 10$ mm, thus defining the vertical thickness of the fluid sample. The external
142 surfaces of the two sapphire windows are in contact with two square aluminium plates with a
143 central circular aperture with a diameter $d = 13$ mm. These plates are meant for hosting two
144 temperature sensors so to measure the temperature as close as possible to the sapphires. The
145 aluminium plates are also in contact with two square Peltier elements (Kryotherm, TB-109-
146 1.4-1.5 CH) which can transport heat by means of a current flow and have the same central
147 circular aperture. The Peltier elements provide/remove the heat necessary to maintain the set-
148 point temperature as driven by two temperature controllers (Wavelength Electronics, LFI-
149 3751) which use a proportional-integrating-derivative feedback system and maintain the
150 temperature of the internal side of each Peltier device constant, with stability better than 1 mK
151 RMS over 1 day. As shown in Fig. 2, all these elements are clamped by means of two
152 aluminium blocks (with the same central circular aperture) in which water coming from a

153 thermostatic controlled bath (Huber, ministat 125), circulates in order to remove the Peltier
154 elements excess heat.



155

156 **Figure 2: 3D drawing of the free-diffusion cell.**

157 External to the stainless steel ring, metallic capillary tubes with external diameter of 1/8 inch
158 and about 50 mm of length (the red stems visible in Fig. 2) are connected to each inlet/outlet.
159 These capillary tubes end with a manual valve each (Swagelok, SS-41GS2), as shown in Fig.
160 3. The sample reservoirs are connected to the valves via flexible capillary tube (same external
161 diameter as the metallic capillary tubes).

162 The cell filling is performed in two main steps. In the first step, the diffusion cell is
163 completely filled with the less dense fluid. In order to do that, the fluid is slowly injected by
164 gravity through the lower part, while air is let out of the outlet pointing to the top. By slightly
165 tilting the cell, the residual air can be completely removed. Attention is paid to avoid any
166 further air inlet while filling the other three capillary tubes. The second step consists of filling
167 the bottom half of the cell with the denser fluid and create a sharp interface between the two
168 fluids. This is achieved by filling the cell simultaneously with the two fluids from the bottom
169 and the top inlets, while the remixed fluid is let out through the two outlets. Once half of the
170 cell is filled with the denser fluid (the volume of fluid to be injected into the cell to fill it by
171 half, taking into account the length and the internal diameter of capillary tubes and the dead

172 volumes is calculated beforehand), a relatively flat horizontal interface between the two fluids
173 is formed. The four valves are simultaneously closed and the free-diffusion process starts.

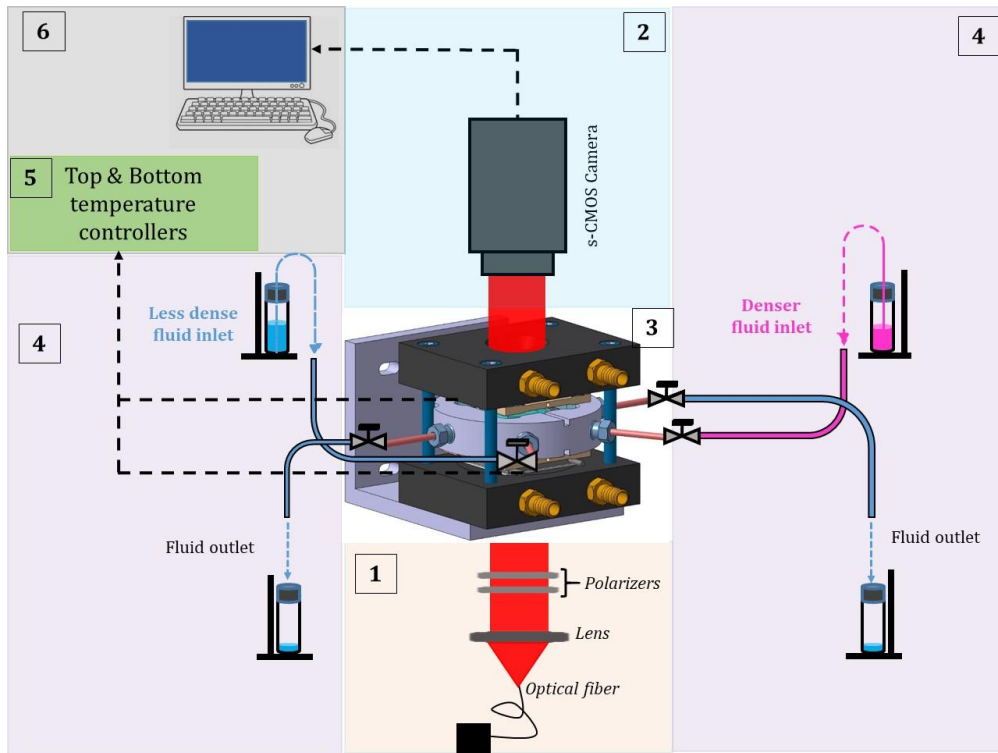
174

175 For the thermodiffusion experiments the stainless steel annulus is replaced by a Viton O-ring
176 with an internal diameter of $d = 25$ mm and thickness of $e = 3$ mm, the other components
177 remain unchanged and capillaries are not necessary. The two sapphire windows are kept apart
178 by four plastic spacers of $h = 2.00 \pm 0.01$ mm, thus defining the liquid layer thickness. The cell
179 is filled by means of two syringe needles punctured through the Viton O-ring. During the
180 filling procedure, the cell is inclined and the fluid is pushed through the bottom syringe while
181 air is removed through the top one. After filling, the two needles are carefully removed and
182 the holes in the O-ring close due to the pressure exercised on it by the sapphire windows. The
183 cell is inserted into the shadowgraph setup once the filling is finished. For any given mean
184 temperature, a temperature difference between the top and the bottom is applied by setting the
185 corresponding temperatures to the Peltier elements. Once the stationary state is reached, i.e.
186 after one diffusive time for the cell, the image recording is started.

187 **2.3. Shadowgraph setup**

188 The shadowgraph optical setup (Fig. 3) involves a super luminescent diode (Super Lumen,
189 SLD MS-261-MP2-SM, $\lambda = 675 \pm 13$ nm), connected to a single-mode optical fiber. The
190 divergent beam at the output of the fiber is collimated by an achromatic doublet lens (focal
191 length $f = 150$ mm, and diameter $\phi = 50.8$ mm). The collimated beam passes through the free-
192 diffusion cell, or the thermodiffusion cell, via two linear polarizers that allow adjusting the
193 average transmitted light intensity, and is supposed to be perpendicular to the interface
194 between the two solutions, in the case of free diffusion experiments, or parallel to the
195 temperature gradient in the case of thermodiffusion experiments. A camera, whose detection
196 plane is positioned at a distance of $z = (12.0 \pm 0.5)$ cm from the sample central plane, collects

197 the sum of the light scattered by the NEFs plus the transmitted one. As a camera sensor, we
 198 use a scientific-CMOS camera (Hamamatsu Digital Camera C13440, ORCA - Flash 4.0 V3)
 199 whose detector size is $s = 13.3$ mm. This camera sensor allows a fast image acquisition
 200 frequency, up to 100 Hz at full frame resolution of 2048×2048 square pixels with a pixel side
 201 of $l_{pix} = 6.5$ μm. Images are acquired in real time by the HCLive (x64) software
 202 program installed in a dedicated PC. In order to have both a good stability of acquisition
 203 frequency and a quick backup of the images, we use 4 Solid-State Drive (SSD) hard disks in
 204 RAID0 configuration.



205

206 **Figure 3: Shadowgraph optical set up summarized in six distinct blocks: 1) optical components; 2) s-**
 207 **CMOS Camera; 3) free-diffusion/thermodiffusion cell; 4) specific filling procedure; 5) temperature**
 208 **controllers; 6) computer equipment.**

209

210 2.4. Dynamic Near field imaging

211 The images acquired in the near field consist of an intensity map $I(\vec{x}, t)$, generated by the
 212 interference on the s-CMOS plane between the portion of the incident beam that has passed
 213 undisturbed through the sample and the beams scattered by the refractive index fluctuations

214 occurring within the sample. Here, \vec{x} and t stand for the position in the image plane and the
 215 time lapsed during the acquisition, respectively. Thanks to the interference of different beams,
 216 the fluctuations in the fluid density, that are proportional to the fluctuations of the fluid
 217 refractive index, are transformed into fluctuations of the light intensity at the detector plane.
 218 Therefore, in order to study the dynamics of the density fluctuations in our samples, we
 219 calculate the Structure Function (SF) of the light intensity, i.e. of the acquired images, by
 220 means of an already proven Differential Dynamic Algorithm (DDA) [33]. The DDA
 221 algorithm consists of the following main steps: first, each recorded image $I(\vec{x}, t)$ is Fourier
 222 transformed in the 2D spatial space of the detector plane to obtain $I(\vec{q}, t) = \mathcal{F}(I(\vec{x}, t))$, then
 223 the Fourier transform (FT) is normalised by dividing it by the zero spatial frequency $i(\vec{q}, t) =$
 224 $I(\vec{q}, t)/I(\vec{0}, t)$ in order to remove the source intensity fluctuations. Then, the differences
 225 between normalized FTs at a given time difference Δt (called correlation time) $\Delta i(\vec{q}, t, \Delta t) =$
 226 $i(\vec{q}, t) - i(\vec{q}, t + \Delta t)$ are calculated. These Δt 's are, of course, multiples of the time delay
 227 dt_{\min} of the recording process, and cannot be larger than the acquisition duration. Finally, the
 228 2D correlation functions are calculated by determining the - square moduli $|\Delta i(\vec{q}, t, \Delta t)|^2$ of
 229 the FT differences, and the individual spatial Fourier transforms of the image differences are
 230 averaged, first over all times t and second over the modulus of the wave number \vec{q} over the
 231 azimuthal angle. The result $\langle |\Delta i(q, \Delta t)|^2 \rangle_{q,t}$ is the SF of the recorded intensity fluctuations. In
 232 order to reduce the computational time to calculate the structure function out of the image
 233 series, we make use of a graphic card with the advantage of the massive parallelization on the
 234 Graphic Processing Unit (GPU) and an in-house developed software [33], [34]. This
 235 experimental quantity requires a physical model for its interpretation. The details of the
 236 theoretical model can be found elsewhere [19], [20]. In the present paper, we just recall the
 237 essential equations used to fit the SF.

238 2.5. Structure function analysis

239 The SF can be related to the power spectrum density fluctuation and the characteristics of the
 240 optical system as follows:

$$\langle |\Delta i(q, \Delta t)|^2 \rangle = 2\{T(q)S(q)[1 - ISF(q, \Delta t)] + B(q, \Delta t)\} \quad (3)$$

241 where $T(q)$ is the optical transfer function of the shadowgraph, $S(q)$ the static power
 242 spectrum of the fluctuations, the product $A(q) = T(q)S(q)$ is called the static structure factor
 243 (independent of the correlation time) and $B(q, \Delta t)$ is the signal background. It includes
 244 different contributions like electronic noise due to the camera and all the acquisition chain and
 245 can be modelled by $B(q, \Delta t) = C(q) + E(q) \cdot \Delta t + F(q) \cdot \Delta t^2$. The parabolic term $F(q) \cdot$
 246 Δt^2 becomes particularly important for the experiments performed in the free-diffusion
 247 configuration, where the system is never at the steady state, so that the background noise
 248 becomes time-dependent. The Intermediate Scattering Function $ISF(q, \Delta t)$ corresponds to the
 249 dynamic part of the SF, that can be described in many cases as the sum of exponential decays
 250 [35]–[37]: $ISF(q, \Delta t) = \sum_i a_i \exp(-\Delta t/\tau_i(q))$, where a_i are the amplitudes of the different
 251 modes with $\sum_i a_i = 1$ and $\tau_i(q)$ the wave-number-dependent relaxation times.

252 During a free-diffusion experiment, the density fluctuations recorded through the
 253 shadowgraph are mostly due to concentration-NEFs (c-NEFs) that are much more intense
 254 (orders of magnitude) than equilibrium temperature and/or concentration fluctuations present
 255 at the same time for the wave number range of our interest. Thus, the ISF is expected to be
 256 well described by a single exponential decay for all wave numbers. Thus, the SF is supposed
 257 to take the following form:

$$\langle |\Delta i(q, \Delta t)|^2 \rangle = 2\left\{A(q)\left[1 - \exp\left(-\frac{\Delta t}{\tau_c(q)}\right)\right] + C(q) + E(q) \cdot \Delta t\right. \\ \left. + F(q) \cdot \Delta t^2\right\} \quad (4)$$

258 where $\tau_c(q)$ is the decay time of the c-NEFs at wave number q .

259 When a stable temperature gradient parallel to the gravity field is applied to a homogenous
 260 binary fluid mixture, a concentration gradient is formed due to the Soret effect [3]. Hence, at
 261 the steady state of a thermodiffusion experiment a suitable expression for the *ISF* can be
 262 provided by the sum of two exponential decays given by the fluctuations of the concentration
 263 plus the fluctuations of the temperature (t-NEFs). The SF is supposed to take the following
 264 form:

$$\begin{aligned} \langle |\Delta i(q, \Delta t)|^2 \rangle = & 2 \left\{ A(q) \left[1 \right. \right. \\ & \left. \left. - \left\{ a \times \exp \left(-\frac{\Delta t}{\tau_T(q)} \right) + (1 - a) \times \exp \left(-\frac{\Delta t}{\tau_c(q)} \right) \right\} \right] \right. \\ & \left. + C(q) + E(q) \cdot \Delta t + F(q) \cdot \Delta t^2 \right\} \end{aligned} \quad (5)$$

265 where $\tau_T(q)$ is the decay time of the t-NEFs at wave number q .
 266 $A(q)$, $\tau_i(q)$, $C(q)$, $E(q)$ and $F(q)$ are the fitting parameters at each wave number. In the case
 267 of a thermodiffusion experiment, if the steady state is fully reached, the term $F(q)$ is
 268 supposed to be negligible. However, we keep it in the fit in order to check the validity of our
 269 hypothesis and to be sure that the steady state has been reached. We use MatLab and an
 270 implemented Levenberg-Marquand non-linear least-square fitting routine [38]. At the end of
 271 the fitting, we proceed to the analysis of the statics of the fluctuations through the static
 272 structure factor $A(q)$, as well as to the analysis of the dynamics of the fluctuations through the
 273 decay times $\tau_i(q)$. In the present paper, we will focus on the dynamics of the fluctuations.

274 **3. Dynamics of the non-equilibrium fluctuations**

275 The details of the theoretical description of the hydrodynamic behaviour of density
 276 fluctuations out-of-equilibrium can be found elsewhere [19], [20], so that here we just recall
 277 the main expressions useful for the experimental data analysis.

278 At intermediate and large wave numbers, in the absence of any convective movement, in the
 279 presence of the gravity force and in the bulk fluid, the decay time of the c-NEFs is given by:

$$\tau_c(q) = \frac{1}{Dq^2 \left[1 + \left(\frac{q_c}{q} \right)^4 \right]} \quad (6)$$

280 where D is the mass diffusion coefficient and q_c the cut-off wave number which defines the
 281 length scale below which the dynamics of the c-NEFs are no longer dominated by diffusion,
 282 but rather by buoyancy. The curve of the decay times as a function of wave numbers looks
 283 like a bell-shape (in log-log scale) and mirrors the presence of two distinct regimes as already
 284 reported in a number of previous publications [25], [26], [39]. The asymptotic behaviour of
 285 Eq. 6 for wave numbers larger than q_c is $\tau_c(q) = 1/Dq^2$ so that the diffusion coefficient D
 286 can be obtained from the fitting of the experimental data points in this region. In the case of a
 287 thermodiffusion experiment, the cut-off wave number is given by the expression [26], [28],
 288 [31], [40]:

$$q_c = \left(\frac{\beta g S_T C_0 (1 - C_0) \Delta T}{h \nu D} \right)^{1/4} \quad (7)$$

289 where β is the mass expansion coefficient of the binary mixture, g the gravitational
 290 acceleration, h is the vertical thickness of the sample, C_0 the equilibrium mass fraction of the
 291 denser component, S_T the Soret coefficient of the denser component, ΔT the difference of
 292 temperature between the top and the bottom of the thermodiffusion cell, and ν the kinematic
 293 viscosity of the binary mixture at the mean temperature of the experiment.

294 During a free-diffusion experiment, the concentration difference between the bottom and the
 295 top of the cell is assumed to remain constant until the diffusive process reaches the cell
 296 boundaries at the diffusive time $\tau_d = (h/2)^2/\pi D$. For times smaller than τ_d the cut-off wave
 297 number is given by the expression [25], [39], [41]:

$$q_c = \left(\frac{\beta g (C_1 - C_2)}{\nu D \sqrt{4\pi D t}} \right)^{1/4} \quad (8)$$

298 where C_1 and C_2 are the concentrations of the denser component, TEG, at the bottom and top
 299 layers in the diffusion cell, respectively. Unlike the thermodiffusion experiment, the cut-off
 300 wave number is time-dependent, following a power law with a $(-1/8 = -0.125)$ exponent.

301 Again, here we recall only the essential equations that are used to model the t-NEFs in the
 302 case of thermodiffusion experiments.

303 At intermediate and large wave numbers, in the absence of convection, in the presence of the
 304 gravity force and in the bulk fluid, the decay time of the t-NEFs is given by:

$$\tau_T(q) = \frac{1}{a_T q^2 \left[1 + \left(\frac{q_T}{q} \right)^4 \right]} \quad (9)$$

305 where a_T is the thermal diffusivity and q_T the thermal cut-off wave number which defines the
 306 length scale below which the dynamics of the t-NEFs is no longer dominated by **heat**
 307 diffusion, but rather by buoyancy. The curve of the decay times as a function of wave
 308 numbers looks similar to the one described for c-NEFS, but, in general, decay times are
 309 shorter, due to the larger value of thermal diffusivity with respect to mass diffusion
 310 coefficient. The asymptotic behaviour of Eq. 9 for wave numbers larger than q_T is $\tau_T(q) =$
 311 $1/(a_T q^2)$ so that the thermal diffusivity a_T can be obtained from the fitting of the
 312 experimental data points in this region.

313 **4. Results and discussion**

314 Mass diffusion and Soret coefficients for the mixture TEG/water at different concentrations
 315 are already known in the literature [42]. The present paper is intended to bring new
 316 measurements of the fluid transport properties at different temperatures. Some of the values
 317 reported here are anticipated in a joint paper about the system TEG/water/ethanol and the

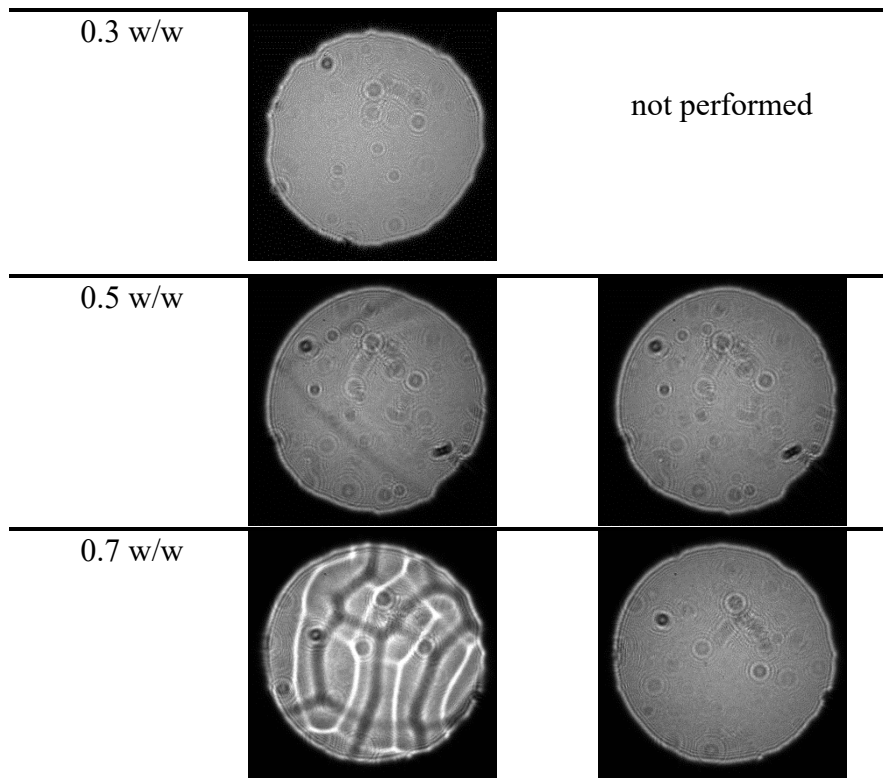
318 associated binary mixtures characterised by different measurement techniques [18]. Here we
 319 provide a full detailed description of the experiments performed in our laboratory by means of
 320 dynamic shadowgraphy and the analysis of NEFs.

321 **4.1. Thermodiffusion experiments**

322 One remarkable property of the TEG/water mixture is that the sign of the Soret coefficient
 323 changes with respect to concentration. This implies that under thermal stress the denser
 324 component (TEG) migrates towards either the hot plate or the cold one. For $C = 0.3$ w/w, the
 325 Soret coefficient is positive, so that the TEG migrates towards the cold plate, while for
 326 concentrations higher than $C = 0.5$ w/w the Soret coefficient is negative in the temperature
 327 range between 15 °C and 40 °C, so that the TEG accumulates at the hot plate. The presence of
 328 a negative Soret coefficient makes it difficult to perform thermodiffusion experiments in the
 329 presence of the gravitational field because, while heating the mixture from above, the density
 330 gradient generated by the concentration one (at the steady state of Soret separation) is
 331 unstable and can induce convection transport process in the system.

332 A first series of qualitative observations at the average temperature of 25 °C have been
 333 performed for three different concentrations by applying to the samples either a stabilizing or
 334 a destabilizing temperature gradient. A stabilizing temperature gradient generates a density
 335 gradient parallel to the gravity acceleration. It is thus obtained by heating from above $\Delta T =$
 336 $+20$ K and with a positive thermal expansion coefficient α . A destabilizing temperature
 337 gradient generates a density gradient anti-parallel to the gravity acceleration. It is thus
 338 obtained by heating from below $\Delta T = -20$ K.

C	$\Delta T = +20$ °C	$\Delta T = -20$ °C
-----	---------------------	---------------------

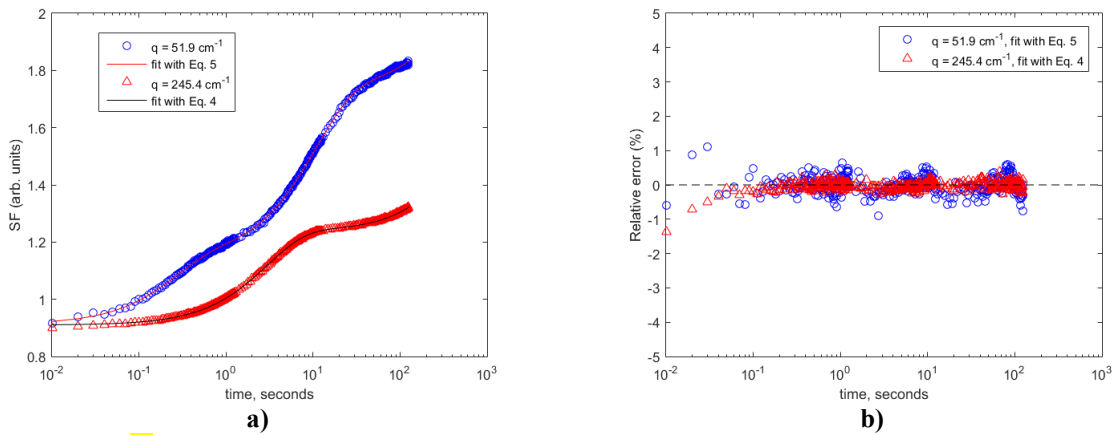


339 **Figure 4: Shadowgraph patterns obtained at a mean temperature of 25 °C after applying different**
 340 **temperature gradients to samples of TEG concentration C (from top to bottom) 0.3, 0.5 and 0.7 w/w. The**
 341 **temperature difference over the cell thickness is of $\Delta T = +20$ °C (heating from above) for the left column,**
 342 **and $\Delta T = -20$ °C (heating from below) for the right one.**
 343

344 As visible in Fig. 4, samples for $C = 0.3, 0.5$ and 0.7 w/w have been stressed by positive and
 345 negative temperature differences while shadowgraph images were recorded in order to
 346 evaluate the presence of convective patterns after reaching the steady state of the Soret
 347 separation. The patterns obtained by heating the samples for $C = 0.3$ w/w from above
 348 (thermally stable), are featureless at the steady state, thus suggesting a stable configuration. In
 349 the patterns visible at $C = 0.5$ w/w slight features appear, thus suggesting a moderate
 350 convective instability taking place within the fluid. This means that the density gradient
 351 originated by the concentration gradient is slightly larger in modulus than the density gradient
 352 generated by the temperature gradient. Finally, strong convective patterns appear in the case
 353 for $C = 0.7$ w/w thus confirming the negative sign of the Soret coefficient for the mixture
 354 TEG/water for concentration of TEG larger than 0.5 w/w.

355 For the cases when a stable configuration was reached at the steady state, series of images
 356 were recorded in order to analyse the NEFs and extract the transport properties of the mixture
 357 as described above. Series of 2500 images of $2048 \times 2048 \text{ pix}^2$ were recorded at 100 Hz, 10 Hz
 358 and 1 Hz at different mean temperatures of 20, 25 and 30 °C.

359 The SFs were calculated and concatenated according to a procedure already presented in our
 360 previous work [36], [37]. The resulting SFs obtained for the concentration of 0.3 w/w of TEG
 361 and the average temperature of 25 °C is shown in Fig. 5a.



362 **Figure 5: a) Concatenated structure functions for different wave numbers of the thermodiffusion**
 363 **experiment carried out at temperature difference of +20 °C, mean temperature of 25 °C and $C = 0.3$ w/w.**
 364 **b) Corresponding relative errors between data points and the theoretical models.**

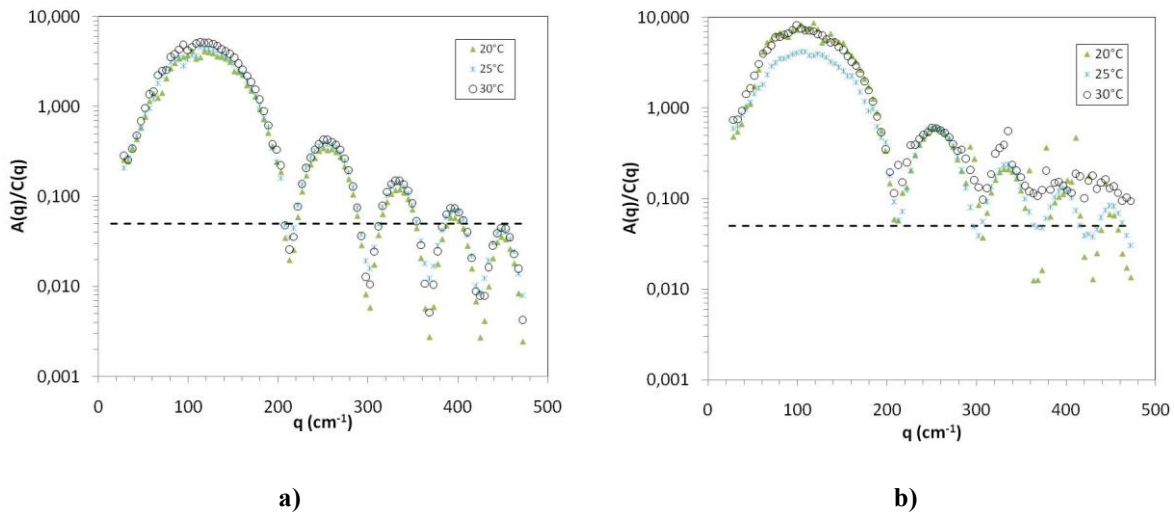
365

366 The minimum accessible wave number is given by $q_{min} = 2\pi/L$, L being the side of the
 367 image in the real space. For the acquired images, $L = 1.33 \text{ cm}$, so that $q_{min} = 4.72 \text{ cm}^{-1}$.

368 The theoretical maximum frequency is $q_{max} = (N_{pix}/2) \cdot q_{min} = 4833 \text{ cm}^{-1}$, N_{pix} being
 369 the number of the pixels along one side of the images.

370 By the analysis of the concatenated SFs, like those shown in Fig. 5a, we could determine that
 371 a double exponential decay is present for wave numbers $q < 200 \text{ cm}^{-1}$, while a simple
 372 exponential decay is present for wave numbers $q > 200 \text{ cm}^{-1}$. In Fig. 5b the relative errors
 373 residuals between the experimental points and the theoretical models for wave numbers $q =$

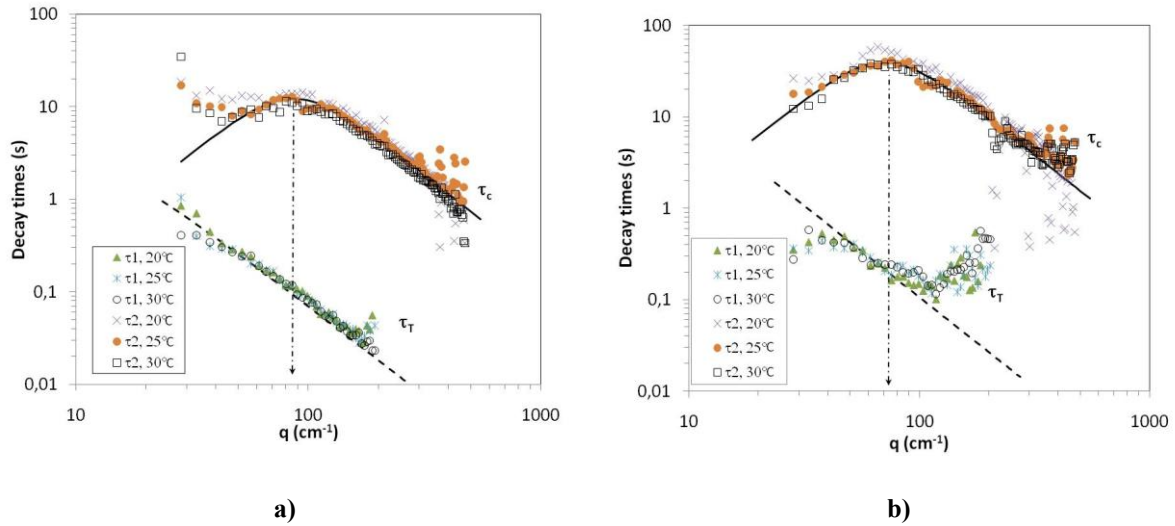
374 51.9 cm⁻¹ and $q = 245.4$ cm⁻¹ are reported. The values are typically smaller than 1% and
 375 random spread around zero, indicating a good match between models and experimental data.
 376 Following these observations, the SFs have been fitted by Eq. 5 for wave numbers smaller
 377 than 200 cm⁻¹ and Eq. 4 for larger ones. As anticipated, the resulting values for the parameters
 378 $E(q)$ and $F(q)$ turned out to be negligible, as an indirect confirmation that the images have
 379 been acquired at the steady state of the thermodiffusion experiment. In this case, the quantity
 380 $A(q)/C(q)$ can be calculated and provides a useful indication of the signal-to-noise ratio of
 381 the measurement. In Fig. 6, the values of such ratio are reported for measurements performed
 382 at $C = 0.3$ and 0.7 w/w and for different average temperatures.



383 **Figure 6: Ratio between the static structure factor and the signal background as a function of the wave**
 384 **number and the mean temperature for the thermodiffusion experiments carried out at temperature**
 385 **difference of a) +20 °C for $C = 0.3$ w/w and b) -20 °C for $C = 0.7$ w/w.**

386
 387 The oscillations visible in the graphs are related to the shadowgraph transfer function $T(q)$
 388 that vanishes at specific wave number. The horizontal line visible in Fig. 6 stands for the
 389 threshold value of 0.05 above which we consider that a shadowgraph measurement cannot
 390 provide reliable results [43], [44]. After such analysis, we decided to perform the fitting in the
 391 common wave number range from 30 to 450 cm⁻¹ for both mixtures, thus spanning more than
 392 one decade in wave numbers.

393 The decay times obtained by fitting data points with the model functions described above are
 394 reported in Fig. 7. In the latter, results are shown for the two concentrations of $C = 0.3$ and 0.7
 395 w/w at the three different temperatures.



396 **Figure 7: Decay times of the t-NEFs (τ_T) and the c-NEFs (τ_c) as a function of the wave number and for**
 397 **three different values of the mean temperature for the thermodiffusion experiments carried out at**
 398 **temperature difference of a) +20 °C for $C = 0.3$ w/w and b) -20 °C for $C = 0.7$ w/w. The continuous lines**
 399 **represent the fitting of the c-NEFs at 25 °C with Eq. 6. The dashed lines represents the fitting of the t-**
 400 **NEFs at 25 °C with the asymptotic behavior of Eq. 9.**

401

402 In both cases, two time decays can be identified for most of the wave numbers. The fastest
 403 modes, corresponding to the smaller value of the time decay, are related to the decay of
 404 thermal fluctuations. Data points obtained for $C = 0.7$ w/w are more scattered than those
 405 obtained for $C = 0.3$ w/w. A possible explanation can be related to the negative Soret
 406 coefficient and the consequent coexistence of a stable density gradient stemming from
 407 concentration profile and an unstable one stemming from the temperature profile.
 408 Nevertheless, two diffusive regimes are clearly visible in both graphs, as indicated by the
 409 decay time behavior proportional to q^{-2} . On the contrary, the gravitational effect is almost not
 410 observable and no clear maximum can be detected for the thermal modes. Nevertheless,
 411 fitting the thermal time decays with the asymptotic behaviour of Eq. 9 can provide a reliable
 412 estimation of the thermal diffusivity a_T . The slowest modes are then related to the decay of

413 concentration fluctuations. For the two concentrations, a mass diffusive mode can be detected
414 as well as the effect of gravity reducing the time decay of NEFs for wave numbers smaller
415 than a characteristic value (q_c). Fitting the concentration time decays with Eq. 6, provides the
416 mass diffusion coefficients D and the cut-off wave numbers q_c at different mean
417 temperatures. At the smallest wavenumbers for $C = 0.3$ w/w, a deviation between the
418 experimental points and the gravity behaviour predicted by Eq. 6 is noticeable. Such
419 behaviour has already been observed on polymer-based systems (slowing-down of the larger
420 fluctuations) [36], [37], and can be attributed to the coupling between different modes, and
421 can also explain why the gravitational behaviour of the thermal fluctuations is not detectable.
422 With the values of D , q_c , β and ν the Soret diffusion coefficients S_T are calculated through
423 Eq. 7. The resulting values of the transport coefficients obtained by thermodiffusion
424 experiments are reported in Table 2.

425 **Table 2. Diffusion coefficients D , cut-off wave number q_c , thermal diffusivity a_T and Soret coefficient S_T**
426 **obtained by thermodiffusion experiments of TEG/water mixtures at different mean temperatures T and**
427 **TEG mass fraction concentration C .**

T (°C)	D ($\times 10^{-6}$ cm ² /s)	q_c (cm ⁻¹)	a_T ($\times 10^{-4}$ cm ² /s)	S_T ($\times 10^{-3}$ K ⁻¹)
$C = 0.3$ w/w				
20	4.79 ± 0.12	86.7 ± 1.1	13.1 ± 0.4	2.3 ± 0.3
25	5.46 ± 0.15	86.8 ± 1.3	13.1 ± 0.2	2.3 ± 0.3
30	6.4 ± 0.3	84 ± 2	13.29 ± 0.13	2.0 ± 0.4
$C = 0.7$ w/w				
20	2.02 ± 0.08	70.7 ± 1.5	9.4 ± 0.2	- 3.8 ± 0.6
25	2.6 ± 0.1	70.3 ± 1.4	9.4 ± 0.4	- 3.9 ± 0.6
30	2.73 ± 0.06	70.5 ± 0.8	9.4 ± 0.4	- 3.4 ± 0.3

428

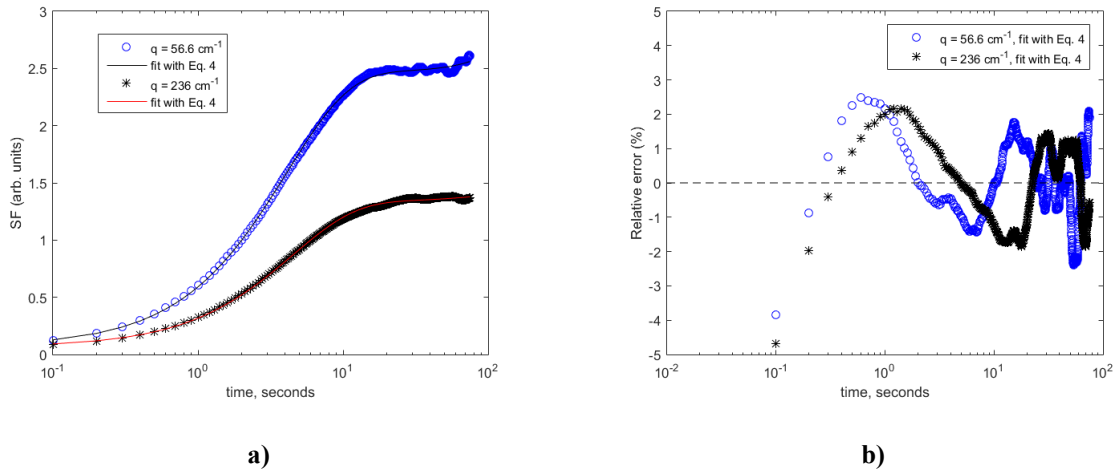
429 Uncertainties for the mass diffusion coefficients, cut-off wave numbers and thermal
430 diffusivities are those given by the fitting routine. Uncertainties for the Soret coefficients are
431 calculated by error propagation. The values reported in Table 2 show that the diffusion
432 coefficient increases with the temperature for the two TEG concentrations, which is a
433 reasonable behaviour as fluid viscosity typically decreases with increasing temperature and
434 the mass diffusion coefficient is inversely proportional to the fluid viscosity, following the
435 Stokes-Einstein relation. Taking into account the uncertainties, the values of the Soret
436 coefficient do not change over the investigated temperature range for $C=0.3$ w/w, and a clear
437 trend is not observed for $C = 0.7$ w/w.

438 **4.2. Free-diffusion experiments**

439 For the concentration $C = 0.5$ w/w it was not possible to obtain a reliable measurement of the
440 mass diffusion coefficient from the thermodiffusion experiments, **due to the negative value of**
441 **the Soret coefficient, close to zero [18]**. Therefore, free-diffusion experiments were performed
442 at the **average** temperatures of 20, 25 and 30 °C. Further experiments were performed in free-
443 diffusion for the concentration $C = 0.7$ w/w in order to confirm the results obtained by
444 thermodiffusion, given the fact that this is the first time that a shadowgraph investigation of
445 NEFs is performed on a sample with negative Soret coefficients to extract its transport
446 coefficients. In the case of a free-diffusion experiment, the diffusion cell is filled as described
447 in section 2.2. Briefly, the diffusion cell is first filled with the less dense solution and
448 subsequently, the less dense and the denser solution fills about half of the cell, the valves are
449 closed and the free-diffusion process starts. In the case of the isothermal diffusion experiment,
450 only one mode is expected to be measured corresponding to the relaxation of c-NEFs in the
451 fluid mixture. The time decays are therefore expected to span a narrower range of time, so
452 that only one series of images of 1024×1024 pix² is acquired at a frequency of 10 Hz. In this
453 simpler case, the SFs are directly calculated by the DDA algorithm without further

454 processing, as shown in Fig. 8a for the average concentration of $C=0.5$ w/w, a difference of
 455 concentration of $\Delta C = C_1 - C_2 = 0.2$ w/w between the two superposed fluid layers, a
 456 homogeneous temperature of 25 °C, and 80 minutes after closing the valves.

457

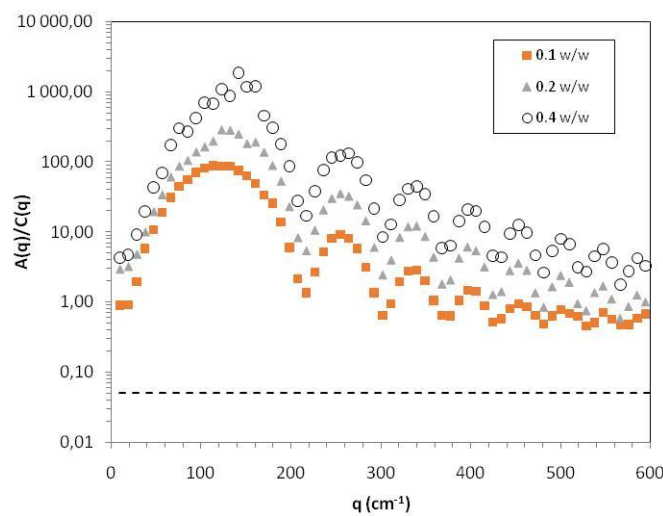


458 **Figure 8: a) Structure function for different wave numbers of the free-diffusion experiment carried out at**
 459 **the mean concentration of $C = 0.5$ w/w, difference of concentration $\Delta C = 0.2$ w/w between the bottom and**
 460 **top layer solutions, mean temperature of 25 °C and 80 minutes after closing the valves.**
 461 **b) Corresponding relative errors between data points and the theoretical models.**

462

463 In Fig. 8b we report the relative errors between the calculated SF and the fitting by a mono-
 464 exponential model of the ISF (Eq. 4). At long correlation times the residuals are slightly
 465 larger, but every time smaller than 3%, so that data points can be fitted through Eq. 4 for the
 466 entire range of wave numbers. In Fig. 9 the signal-to-noise ratio is shown for the sample with
 467 $C = 0.5$ w/w and the homogeneous temperature $T = 25$ °C for images taken 80 minutes after
 468 closing the inlet/outlet valves. The values are reported for three different values of the
 469 concentration difference $\Delta C = 0.1, 0.2$ and 0.4 w/w. By comparing Fig. 6 and 9, it is evident
 470 that the signal obtained in the case of free-diffusion experiments is much larger than the one
 471 obtained in the thermodiffusion experiments. That is due to the fact that the overall signal
 472 intensity is proportional to the square of the density gradient, that is much larger in the free-

473 diffusion case due to the different shape of the concentration profile. The optical signal,
 474 however, is integrated over the entire fluid vertical thickness, which reduces the overall
 475 difference in signal intensity. As visible from Fig. 9, the signal also increases with increasing
 476 concentration difference and distance for ΔC between 0.1 and 0.2 w/w. However, it is
 477 approximately the same in a log-log graph whatever the distance for ΔC between 0.2 and
 478 0.4 w/w, which is coherent with a quadratic dependence of the signal to the concentration
 479 difference.



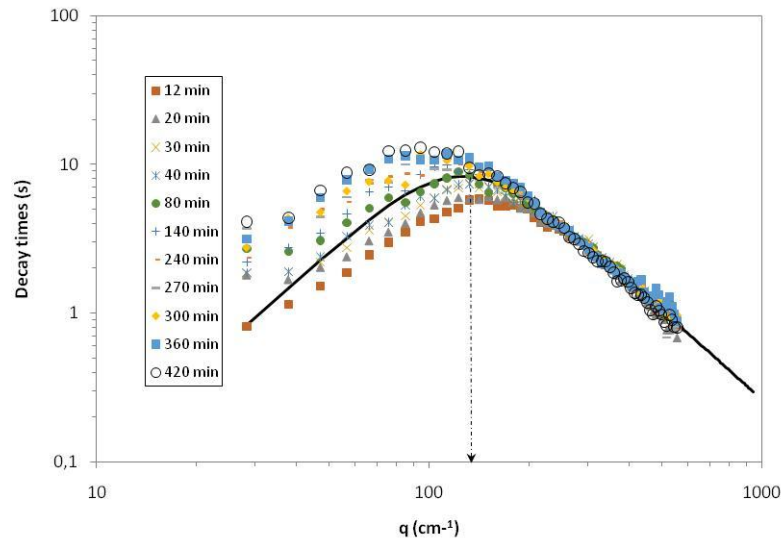
480

481 **Figure 9: Ratio between the static structure factor and the signal background as a function of the wave**
 482 **number for the free-diffusion experiments carried out at mean concentration of $C = 0.5$ w/w, and for**
 483 **different concentration differences between the bottom and the top layers, at 25 °C and 80 minutes after**
 484 **closing the valves.**

485

486 In the case of free-diffusion experiments, we decided to further analyse data points in the
 487 wave number range from 30 to 600 cm^{-1} , within which the signal-to-noise ratio indicator
 488 keeps above the threshold. In Fig. 10 we report the decay times obtained from fitting the SFs
 489 as a function of the wave number q and for different times after closing the inlet/outlet valves.
 490 The graph corresponds to a sample with $C = 0.5$ w/w, $\Delta C = 0.2$ w/w and $T = 25$ °C. As stated
 491 before, only one mode can be detected corresponding to the decay of c-NEFs. By fitting the

492 decay times through Eq. 6 we can obtain a measurement of the roll off wave number q_c and
 493 the mass diffusion coefficient D .

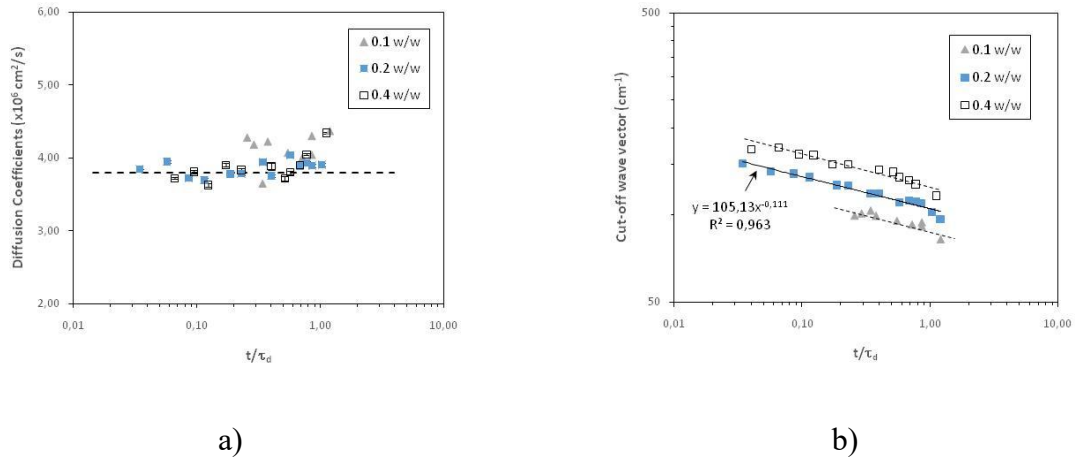


494

495 **Figure 10 : Decay times of the c-NEFs as a function of the wave numbers for different times after closing**
 496 **the inlet/outlet valves for the free-diffusion experiment carried out at $C = 0.5$ w/w, difference of**
 497 **concentration $\Delta C = 0.2$ w/w and $T = 25$ °C. The continuous black line corresponds to the curve got by**
 498 **fitting Eq. 6 to data points obtained 80 minutes after starting the free-diffusion experiment.**

499

500 For all the times, the relaxation time curve has a bell-shape in the log-log plot of τ vs. q . As
 501 already reported in a number of publications, the right part of such curves for large wave
 502 numbers corresponds to the diffusive regime of c-NEFs. All curves collapse onto a single one
 503 for large wave numbers, because the mass diffusion coefficient remains constant during the
 504 free-diffusion process. This can be clearly observed also in Fig. 11-a, where the mass
 505 diffusion coefficients obtained after fitting time decays through Eq. 6 are shown as a function
 506 of the normalised time (i.e. t/τ_d , τ_d calculated using reference values of D). Moreover, the
 507 diffusion coefficient does not change with respect to the applied concentration difference ΔC .
 508 All data shown in Fig. 11 are relative to the average concentration $C = 0.5$ w/w at $T = 25$ °C.
 509 On the contrary, the position of the maximum of the decay time bell-shape, q_c , decreases with
 510 time, as shown Fig. 11-b.



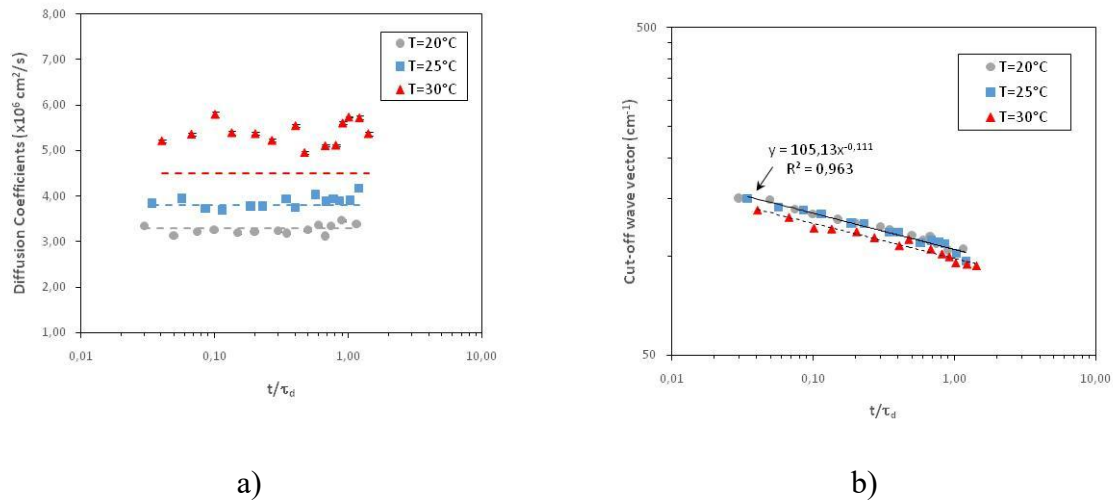
512 **Figure 11: a) Mass diffusion coefficient D and b) cut-off wave number q_c as a function of the normalized**
 513 **time for different concentration differences for the free-diffusion experiments carried out at $C = 0.5$ w/w**
 514 **and $T = 25$ °C.**

515

516 The values obtained for the mass diffusion coefficient D are nicely centred around the
 517 literature value obtained by Optical Beam Deflection (OBD) [18], that is represented by a
 518 horizontal dashed line in Fig. 11-a. The values obtained for $\Delta C = 0.1$ w/w are somewhat more
 519 scattered, which mirrors the smaller signal-to-noise ratio, also visible in Fig.9. Moreover, the
 520 measurement error is increased for times close to the diffusive time of the cell, because, again,
 521 the signal-to-noise ratio decreases due to the decrease of the concentration gradient. The
 522 values obtained for the mass diffusion coefficient remain almost constant as a function of time
 523 and do not depend on the concentration difference imposed at the beginning of the
 524 experiment. Conversely, the cut-off wave number decreases with time and with the
 525 concentration difference according to Eq. 8. Fitting data point with a power law and free
 526 exponent provides a value of -0.11, rather close to the theoretical value of -0.125.

527 The experiments reported in Fig. 12 have been performed with average concentration $C = 0.5$
 528 w/w and concentration difference $\Delta C = 0.2$ w/w. In Fig. 12-a we report the values of the mass
 529 diffusion coefficient and the cut-off wave number as a function of the normalised time and for

530 different values of the homogeneous temperature. In Fig. 12-b we report the values of the cut-
 531 off wave number as a function of the normalized time in the same conditions.



532 **Figure 12 a) Mass diffusion coefficient and b) cut-off wave number as a function of the normalized time**
 533 **for different temperatures for the free-diffusion experiments with $C = 0.5$ w/w and $\Delta C = 0.2$ w/w.**

534
 535 In Fig. 12-a, the horizontal dashed lines provide a visual reference of the values of the mass
 536 diffusion coefficient obtained by OBD and reported in the literature [18]. The data points for
 537 $T = 20$ and 25 °C are in very good agreement with the literature values, however those
 538 obtained at 30 °C show a 10% difference with respect to the literature one. In Fig. 12-b we
 539 can see that the wave numbers follow a power law dependence upon reduced time with an
 540 exponent close to the theoretical value of -0.125 for all the three investigated temperatures.

541 In Table 3 we provide the obtained values of the mass diffusion coefficients as obtained by
 542 the free-diffusion experiments performed at the two average concentrations of $C = 0.5$ and 0.7
 543 w/w, at the three different homogeneous temperatures of $T = 20, 25$ and 30 °C. For the
 544 average concentration of $C = 0.7$ w/w, the studied concentration difference between bottom
 545 and top solutions was $\Delta C = 0.2$ w/w. The corresponding mass diffusion coefficients obtained
 546 at different temperatures are consistent or even compatible to those summarized in Table 2 for
 547 the same TEG concentration of 0.7 w/w.

548

549 **Table 3. Mass diffusion coefficients D obtained by free-diffusion experiments at mean concentration C in**
550 **mass fraction of TEG and homogeneous temperature T .**

$D (\times 10^{-6} \text{ cm}^2/\text{s})$		
$T (\text{°C})$	$C = 0.5 \text{ w/w}$	$C = 0.7 \text{ w/w}$
20	3.27 ± 0.10	2.15 ± 0.16
25	3.86 ± 0.14	2.32 ± 0.06
30	5.4 ± 0.3	3.00 ± 0.13

551

552 The uncertainties reported in Table 3 correspond to the standard deviation with respect to the
553 average value including the measurements obtained at different normalised times. In the case
554 of the measurements performed at $C = 0.5 \text{ w/w}$, we averaged data obtained for $\Delta C = 0.2$ and
555 0.4 w/w .

556 5. Conclusion

557 In this paper, we have measured the mass diffusion and the thermodiffusion coefficients of
558 triethylene glycol and water binary mixtures at different concentrations and average
559 temperatures. Up to our best knowledge, this is the first time that the method combining
560 dynamic shadowgraphy and the analysis of non-equilibrium fluctuations is used to measure
561 the transport properties of a fluid mixture in a free-diffusion experiment. It is also the first
562 time that the method is applied to measure the mass diffusion and the Soret coefficients in a
563 thermodiffusion experiment for a sample of negative Soret coefficient as it is the case for the
564 triethylene glycol/water mixture at $C = 0.7 \text{ w/w}$.

565 The obtained values of mass diffusion coefficient are consistent with data available in the
566 literature for the range of temperature investigated in this study from 20 to 30 °C. The mass
567 diffusion coefficients of 0.7 w/w triethylene glycol/water mixture measured at different

568 temperatures through free-diffusion experiments are consistent with those determined by
569 thermodiffusion experiments. An increase of the mass diffusion coefficient as a function of
570 the average temperature is detected. On the other hand, the thermodiffusion coefficient
571 appears to be independent of the average temperature of the sample at 0.3 w/w triethylene
572 glycol concentration. Soret coefficients have been determined with a relative uncertainty of
573 10% without prior knowledge of optical contrast factors.

574

575

576 **Acknowledgements**

577 This work was developed in the framework of the cooperative project DCMIX (AO-2009-
578 0858/1056) of the European Space Agency (ESA) and the Russian Space Agency
579 (Roscosmos). The shadowgraphy measurements are supported by the ESA project GIANT
580 FLUCTUATIONS and the ESA-MAP project TechNES (Grant 4000128933/19/NL/PG). We
581 acknowledge financial support from the CNES and from the E2S UPPA Hub Newpores and
582 the Industrial Chair CO2ES supported by the Investissements d’Avenir French programme
583 managed by ANR (ANR-16-IDEX-0002), and BRGM and TotalEnergies. L. García-
584 Fernández is thankful to Comunidad de Madrid for the financial support of the postdoctoral
585 researcher contract “Atracción de Talento Investigador (2019-T2/AMB-15912)”.

586

587 **Author contributions statement**

588 H.B., M.A., A.L. and F.C. conceived the project and the experiments. A.T.N. conducted the
589 experiments. H.B., A.T.N., L.G.F. and F.C. wrote the manuscript. All the authors analyzed
590 and discussed the content of the paper.

591

- 594 [1] F. Montel, J. Bickert, A. Lagisquet, and G. Galliero, ‘Initial state of petroleum reservoirs: A
595 comprehensive approach’, *Journal of Petroleum Science and Engineering*, vol. 58, no. 3, pp. 391–
596 402, Sep. 2007, doi: 10.1016/j.petrol.2006.03.032.
- 597 [2] H. Guo, Q. Zhou, Z. Wang, and Y. Huang, ‘Soret effect on the diffusion of CO₂ in aqueous
598 solution under high-pressure’, *International Journal of Heat and Mass Transfer*, vol. 117, pp.
599 966–971, Feb. 2018, doi: 10.1016/j.ijheatmasstransfer.2017.10.058.
- 600 [3] W. Köhler and K. I. Morozov, ‘The Soret Effect in Liquid Mixtures – A Review’, *Journal of Non-
601 Equilibrium Thermodynamics*, vol. 41, no. 3, pp. 151–197, Jul. 2016, doi: 10.1515/jnet-2016-
602 0024.
- 603 [4] J. K. Platten *et al.*, ‘Benchmark values for the Soret, thermal diffusion and diffusion coefficients
604 of three binary organic liquid mixtures’, *Philosophical Magazine*, vol. 83, no. 17–18, pp. 1965–
605 1971, Jan. 2003, doi: 10.1080/0141861031000108204.
- 606 [5] H. Bataller, T. Triller, B. Pur, W. Köhler, J. M. Ortiz de Zárate, and F. Croccolo, ‘Dynamic
607 analysis of the light scattered by the non-equilibrium fluctuations of a ternary mixture of
608 polystyrene-toluene-n-hexane’, *Eur. Phys. J. E*, vol. 40, no. 3, p. 35, Mar. 2017, doi:
609 10.1140/epje/i2017-11522-8.
- 610 [6] H. Bataller, C. Giraudet, F. Croccolo, and J. M. Ortiz de Zárate, ‘Analysis of Non-Equilibrium
611 Fluctuations In A Ternary Liquid Mixture’, *Microgravity Sci. Technol.*, vol. 28, no. 6, pp. 611–
612 619, Dec. 2016, doi: 10.1007/s12217-016-9517-6.
- 613 [7] M. M. Bou-Ali *et al.*, ‘Benchmark values for the Soret, thermodiffusion and molecular diffusion
614 coefficients of the ternary mixture tetralin+isobutylbenzene+n-dodecane with 0.8-0.1-0.1 mass
615 fraction’, *Eur. Phys. J. E*, vol. 38, no. 4, Art. no. 4, Apr. 2015, doi: 10.1140/epje/i2015-15030-7.
- 616 [8] A. Ahadi, S. V. Varenbergh, and M. Z. Saghir, ‘Measurement of the Soret coefficients for a
617 ternary hydrocarbon mixture in low gravity environment’, *J. Chem. Phys.*, vol. 138, no. 20, p.
618 204201, May 2013, doi: 10.1063/1.4802984.
- 619 [9] A. Mialdun, I. Ryzhkov, O. Khlybov, T. Lyubimova, and V. Shevtsova, ‘Measurement of Soret
620 coefficients in a ternary mixture of toluene–methanol–cyclohexane in convection-free
621 environment’, *J. Chem. Phys.*, vol. 148, no. 4, p. 044506, Jan. 2018, doi: 10.1063/1.5017716.
- 622 [10] A. Mialdun and V. Shevtsova, ‘Temperature dependence of Soret and diffusion coefficients for
623 toluene–cyclohexane mixture measured in convection-free environment’, *J. Chem. Phys.*, vol.
624 143, no. 22, p. 224902, Dec. 2015, doi: 10.1063/1.4936778.
- 625 [11] T. Triller *et al.*, ‘Thermodiffusion in Ternary Mixtures of Water/Ethanol/Triethylene Glycol: First
626 Report on the DCMIX3-Experiments Performed on the International Space Station’, *Microgravity
627 Sci. Technol.*, vol. 30, no. 3, pp. 295–308, May 2018, doi: 10.1007/s12217-018-9598-5.
- 628 [12] M. Touzet, G. Galliero, V. Lazzeri, M. Z. Saghir, F. Montel, and J.-C. Legros, ‘Thermodiffusion:
629 From microgravity experiments to the initial state of petroleum reservoirs’, *Comptes Rendus
630 Mécanique*, vol. 339, no. 5, pp. 318–323, May 2011, doi: 10.1016/j.crme.2011.03.008.
- 631 [13] G. Galliero *et al.*, ‘Thermodiffusion in multicomponent n-alkane mixtures’, *npj Microgravity*, vol.
632 3, no. 1, pp. 1–7, Aug. 2017, doi: 10.1038/s41526-017-0026-8.
- 633 [14] S. VanVaerenbergh, S. Srinivasan, and M. Z. Saghir, ‘Thermodiffusion in multicomponent
634 hydrocarbon mixtures: experimental investigations and computational analysis’, *J. Chem. Phys.*,
635 vol. 131, no. 11, p. 114505, Sep. 2009, doi: 10.1063/1.3211303.
- 636 [15] G. Galliero *et al.*, ‘Impact of Thermodiffusion on the Initial Vertical Distribution of Species in
637 Hydrocarbon Reservoirs’, *Microgravity Sci. Technol.*, vol. 28, no. 2, pp. 79–86, May 2016, doi:
638 10.1007/s12217-015-9465-6.
- 639 [16] P. Baaske *et al.*, ‘The NEUF-DIX space project - Non-EquilibriUm Fluctuations during Diffusion
640 in compleX liquids’, *Eur. Phys. J. E*, vol. 39, no. 12, Art. no. 12, Dec. 2016, doi:
641 10.1140/epje/i2016-16119-1.
- 642 [17] M. Braibanti *et al.*, ‘European Space Agency experiments on thermodiffusion of fluid mixtures in
643 space’, *Eur. Phys. J. E*, vol. 42, no. 7, p. 86, Jul. 2019, doi: 10.1140/epje/i2019-11849-0.

- 644 [18]M. Schraml *et al.*, ‘The Soret coefficients of the ternary system water/ethanol/triethylene glycol
645 and its corresponding binary mixtures’, *Eur. Phys. J. E*, vol. 44, no. 10, p. 128, Oct. 2021, doi:
646 10.1140/epje/s10189-021-00134-6.
- 647 [19]J. M. Ortiz de Zárate and J. V. Sengers, ‘Hydrodynamic Fluctuations in Fluids and Fluid Mixtures
648 - 1st Edition’. [https://www.elsevier.com/books/hydrodynamic-fluctuations-in-fluids-and-fluid-](https://www.elsevier.com/books/hydrodynamic-fluctuations-in-fluids-and-fluid-mixtures/ortiz-de-zarate/978-0-444-51515-5)
649 [mixtures/ortiz-de-zarate/978-0-444-51515-5](https://www.elsevier.com/books/hydrodynamic-fluctuations-in-fluids-and-fluid-mixtures/ortiz-de-zarate/978-0-444-51515-5) (accessed Sep. 30, 2021).
- 650 [20]F. Croccolo, J. M. Ortiz de Zárate, and J. V. Sengers, ‘Non-local fluctuation phenomena in
651 liquids’, *Eur. Phys. J. E*, vol. 39, no. 12, p. 125, Dec. 2016, doi: 10.1140/epje/i2016-16125-3.
- 652 [21]A. Vailati and M. Giglio, ‘Giant fluctuations in a free diffusion process’, *Nature*, vol. 390, no.
653 6657, pp. 262–265, Nov. 1997, doi: 10.1038/36803.
- 654 [22]P. N. Segrè, R. Schmitz, and J. V. Sengers, ‘Fluctuations in inhomogeneous and nonequilibrium
655 fluids under the influence of gravity’, *Physica A: Statistical Mechanics and its Applications*, vol.
656 195, no. 1, pp. 31–52, Apr. 1993, doi: 10.1016/0378-4371(93)90252-Y.
- 657 [23]P. N. Segrè and J. V. Sengers, ‘Nonequilibrium fluctuations in liquid mixtures under the influence
658 of gravity’, *Physica A: Statistical Mechanics and its Applications*, vol. 198, no. 1, pp. 46–77, Sep.
659 1993, doi: 10.1016/0378-4371(93)90183-5.
- 660 [24]E. Bouty, ‘CH. SORET. — Sur l’état d’équilibre que prend, au point de vue de sa concentration,
661 une dissolution saline primitivement homogène, dont deux parties sont portées à des températures
662 différentes; Archives de Genève, 3e periode, t. II, p. 48; 1879’, *J. Phys. Theor. Appl.*, vol. 9, no. 1,
663 pp. 331–332, 1880, doi: 10.1051/jphystap:018800090033101.
- 664 [25]F. Croccolo, D. Brogioli, A. Vailati, M. Giglio, and D. S. Cannell, ‘Nondiffusive decay of
665 gradient-driven fluctuations in a free-diffusion process’, *Phys. Rev. E*, vol. 76, no. 4, p. 041112,
666 Oct. 2007, doi: 10.1103/PhysRevE.76.041112.
- 667 [26]F. Croccolo, H. Bataller, and F. Scheffold, ‘A light scattering study of non equilibrium
668 fluctuations in liquid mixtures to measure the Soret and mass diffusion coefficient’, *J. Chem.*
669 *Phys.*, vol. 137, no. 23, p. 234202, Dec. 2012, doi: 10.1063/1.4771872.
- 670 [27]W. Wu, J. H. Jander, M. H. Rausch, A. P. Fröba, and C. Giraudet, ‘Simultaneous determination of
671 multiple transport properties over a wide range of temperatures and pressures from the analysis of
672 non-equilibrium fluctuations by the shadowgraph method’, *J. Chem. Phys.*, vol. 153, no. 14, p.
673 144201, Oct. 2020, doi: 10.1063/5.0024503.
- 674 [28]C. Giraudet, H. Bataller, and F. Croccolo, ‘High-pressure mass transport properties measured by
675 dynamic near-field scattering of non-equilibrium fluctuations’, *Eur. Phys. J. E*, vol. 37, no. 11, p.
676 107, Nov. 2014, doi: 10.1140/epje/i2014-14107-1.
- 677 [29]F. Croccolo and D. Brogioli, ‘Quantitative Fourier analysis of schlieren masks: the transition from
678 shadowgraph to schlieren’, *Appl. Opt., AO*, vol. 50, no. 20, pp. 3419–3427, Jul. 2011, doi:
679 10.1364/AO.50.003419.
- 680 [30]S. P. Trainoff and D. S. Cannell, ‘Physical optics treatment of the shadowgraph’, *Physics of*
681 *Fluids*, vol. 14, no. 4, pp. 1340–1363, Apr. 2002, doi: 10.1063/1.1449892.
- 682 [31]I. Lizarraga, C. Giraudet, F. Croccolo, M. M. Bou-Ali, and H. Bataller, ‘Mass Diffusion and
683 Thermal Diffusivity of the Decane-pentane Mixture Under High Pressure as a Ground-based
684 Study for SCCO Project’, *Microgravity Sci. Technol.*, vol. 28, no. 5, pp. 545–552, Oct. 2016, doi:
685 10.1007/s12217-016-9506-9.
- 686 [32]F. Croccolo, D. Brogioli, and A. Vailati, ‘Cylindrical flowing-junction cell for the investigation of
687 fluctuations and pattern-formation in miscible fluids’, *Review of Scientific Instruments*, vol. 90,
688 no. 8, p. 085109, Aug. 2019, doi: 10.1063/1.5112778.
- 689 [33]G. Cerchiari, F. Croccolo, F. Cardinaux, and F. Scheffold, ‘Note: Quasi-real-time analysis of
690 dynamic near field scattering data using a graphics processing unit’, *Review of Scientific*
691 *Instruments*, vol. 83, no. 10, p. 106101, Oct. 2012, doi: 10.1063/1.4755747.
- 692 [34]M. Norouzisadeh, M. Chraga, G. Cerchiari, and F. Croccolo, ‘The modern structurator: Increased
693 performance for calculating the structure function.’, *submitted*.
- 694 [35]J. M. Ortiz de Zárate, C. Giraudet, H. Bataller, and F. Croccolo, ‘Non-equilibrium fluctuations
695 induced by the Soret effect in a ternary mixture’, *Eur. Phys. J. E*, vol. 37, no. 8, Art. no. 8, Aug.
696 2014, doi: 10.1140/epje/i2014-14077-2.

- 697 [36]F. Croccolo, L. García-Fernández, H. Bataller, A. Vailati, and J. M. Ortiz de Zárate, ‘Propagating
698 modes in a binary liquid mixture under thermal stress’, *Phys. Rev. E*, vol. 99, no. 1, p. 012602,
699 Jan. 2019, doi: 10.1103/PhysRevE.99.012602.
- 700 [37]L. García-Fernández, P. Fruton, H. Bataller, J. M. Ortiz de Zárate, and F. Croccolo, ‘Coupled non-
701 equilibrium fluctuations in a polymeric ternary mixture’, *Eur. Phys. J. E*, vol. 42, no. 9, Art. no. 9,
702 Sep. 2019, doi: 10.1140/epje/i2019-11889-4.
- 703 [38]D. J. Higham and N. J. Higham, *MATLAB Guide, Third Edition*. SIAM, 2016.
- 704 [39]F. Croccolo, D. Brogioli, A. Vailati, M. Giglio, and D. S. Cannell, ‘Use of dynamic schlieren
705 interferometry to study fluctuations during free diffusion’, *Appl. Opt., AO*, vol. 45, no. 10, pp.
706 2166–2173, Apr. 2006, doi: 10.1364/AO.45.002166.
- 707 [40]I. Lizarraga, F. Croccolo, H. Bataller, and M. M. Bou-Ali, ‘Soret coefficient of the n-dodecane-n-
708 hexane binary mixture under high pressure’, *Eur. Phys. J. E*, vol. 40, no. 3, Art. no. 3, Mar. 2017,
709 doi: 10.1140/epje/i2017-11520-x.
- 710 [41]F. Croccolo, D. Brogioli, A. Vailati, M. Giglio, and D. S. Cannell, ‘Effect of Gravity on the
711 Dynamics of Nonequilibrium Fluctuations in a Free-Diffusion Experiment’, *Annals of the New
712 York Academy of Sciences*, vol. 1077, no. 1, pp. 365–379, 2006, doi: 10.1196/annals.1362.030.
- 713 [42]J. C. Legros *et al.*, ‘Investigation of Fickian diffusion in the ternary mixtures of water–ethanol–
714 triethylene glycol and its binary pairs’, *Phys. Chem. Chem. Phys.*, vol. 17, no. 41, pp. 27713–
715 27725, Oct. 2015, doi: 10.1039/C5CP04745E.
- 716 [43]K. He, M. Spannuth, J. C. Conrad, and R. Krishnamoorti, ‘Diffusive dynamics of nanoparticles in
717 aqueous dispersions’, *Soft Matter*, vol. 8, no. 47, pp. 11933–11938, Nov. 2012, doi:
718 10.1039/C2SM26392K.
- 719 [44]M. S. Safari, M. A. Vorontsova, R. Poling-Skutvik, P. G. Vekilov, and J. C. Conrad, ‘Differential
720 dynamic microscopy of weakly scattering and polydisperse protein-rich clusters’, *Phys. Rev. E*,
721 vol. 92, no. 4, p. 042712, Oct. 2015, doi: 10.1103/PhysRevE.92.042712.
- 722